INERTIAL OSCILLATIONS IN THE SOLAR CONVECTION ZONE. I. SPHERICAL SHELL MODEL

D. B. GUENTHER[1] AND PETER A. GILMAN
High Altitude Observatory, National Center for Atmospheric Research,[2] Boulder, Colorado
Received 1984 November 26; accepted 1985 February 13

ABSTRACT

Axisymmetric inertial oscillations, oscillations in which the Coriolis force provides the principal restoring force, are investigated theoretically for a model solar convection zone. The fluid flow equations, describing such oscillations in an adiabatically stratified, differentially rotating spherical shell, are written in the form of a modified eigenvalue problem. The modified eigenvalue equations in finite-difference form are numerically solved on a staggered grid (19 points in radius by 43 points in latitude). Solutions, each consisting of 817 different meridional stream functions (Ψ) and corresponding zonal velocities (U), are obtained for several combinations of convection zone depth and rotation profile. We discuss general characteristics of the solutions, as revealed in contour plots of the stream functions and U-velocities. A low-latitude frequency (ω) versus latitudinal wavenumber (k) diagram is defined for the oscillations. Ridge structure in this ω-k diagram is found to be sensitive to both the convection zone's depth and its rotation profile. Since the two effects are distinct, observing the oscillations with sufficient frequency and spatial resolution to resolve the ridges in the ω-k diagram will enable an independent determination of the convective envelope's depth and its rotation profile. We discuss the possibilities of observing these modes with the Fourier Tachometer.

Subject headings: Sun: interior — Sun: oscillations

I. INTRODUCTION

The solar oscillation spectrum has the potential to tell us a great deal about the Sun's interior. Interpreting the oscillation spectrum unambiguously, however, is extremely difficult regardless of the method used. One can approach the problem of interpreting the oscillation spectrum either directly or indirectly.

In a direct approach, trial oscillation spectra are constructed based upon a variety of solar models (Christensen-Dalsgaard, Gough, and Morgan 1979; Iben and Mahaffy 1976). If a specific trial spectrum matches the solar oscillation spectrum, one hopes that the corresponding solar model matches the true solar structure. Because the solar models are calculated using stellar evolution programs, the success of the direct method is determined by the correctness of the stellar evolution program. Unfortunately, the structure of the convection zone, where the frequencies of the solar oscillations are mainly determined, is modeled by one of the weakest aspects of stellar evolution theory: mixing-length theory (used to model convective energy transport). Nonetheless, the direct method has the advantage that the scientist, constructing the models, can intelligently select the models to be tested (the bias of the scientist is an obvious disadvantage).

In recent years, indirect approaches have become popular. Here one tries to reconstruct the environment in which the oscillations exist, by inverting the pulsation equations so that, for example, one can solve for the run of density and pressure in terms of a given frequency spectrum. The mathematical theory for performing the inversion has already been developed by geophysicists (Backus and Gilbert 1968) and applied to the Sun (Duvall and Harvey 1984; Duvall *et al.* 1984). There are problems. Since the oscillation spectrum is not complete (all possible solar oscillations have not been observed), the inversion method cannot give a complete description of the Sun's interior. Either the results are ambiguous, i.e. more than one inverted solution is found, or the inverted solution uniquely describes only a specific region of the Sun.

Since neither approach can give a complete picture of the solar interior, it seems prudent to use a wide variety of methods to probe the interior. In this work we describe a relatively ignored family of solar oscillations, called inertial oscillations, which we show are sensitive (independently) to both the depth and the rotation profile of the convection zone. If these modes can be observed (see § IV), they will provide an independent determination of the convection zone depth and rotation frequency profile, as a function of radius (and latitude).

A fluid element in a noninertial reference frame which is perturbed from its equilibrium position experiences forces (in addition to the usual rest-frame forces) which are directly related to the pseudoforces of the noninertial reference frame. In particular, in a rotating reference frame the displaced fluid volume experiences a Coriolis force. In general, if the pseudoforces act to restore the equilibrium configuration, oscillations can exist. In the example of the rotating frame the oscillation frequencies are of the same order as the rotation frequency. Oscillations of this type, called inertial oscillations, have been extensively studied in applications related to the Earth's atmosphere and oceans (Tolstoy 1963; Stern 1963; Bretherton 1964; Stewartson 1972; Munk and Phillips 1968). The general theory of inertial oscillation is discussed by Greenspan (1968, p. 40). The literature on inertial oscillations (induced by rotation) in stellar physics is scarce. Some work, however, has been carried out recently by Clement (1981, 1984). Because of the numerical method he used, his investigations were primarily limited to a few low-order inertial modes.

195

Related work on so-called toroidal or *R*-modes, e.g., Saio (1982), looks at a distinctly different class of oscillations from that which we will study. In particular, such analyses assume that the radial motions are very small compared with those in spherical surfaces. This is appropriate to a stably stratified radiative zone, but not to a convection zone, where there is no negative buoyancy force to oppose radial motions. Conversely, the modes we will study cannot occur in a stably stratified zone, because their radial motions will be largely suppressed. Consequently a boundary condition of no radial motion is the appropriate one to take at the bottom of the convection zone.

To investigate axisymmetric inertial oscillations, we have rewritten the fluid flow equations in the form of a modified eigenvalue equation. The finite-difference form of the modified eigenvalue equation is solved numerically to obtain the complete spectrum of inertial oscillation modes for the Sun. We are able to determine the structure and frequencies of these oscillations as a function of convection zone depth and rotation profile.

Because the modes are confined to a spherical shell, their very complicated spatial structure cannot be easily classified within the formalism of spherical harmonics. We have, however, found that the spatial structure of the modes in the equatorial regions is reasonably well defined and can be interpreted with a simple cylindrical coordinate model. This model will be discussed in more detail by Gilman and Guenther (1985, hereafter Paper II).

A frequency (ω) versus low-latitude latitudinal wavenumber (k) diagram is introduced as an aid to understanding the general behavior of the modes. The low-latitude latitudinal wavenumber is defined as the average wavenumber of the oscillation in the region $\pm 15°$ latitude from the equator. (The low-latitude ω-k diagram is analogous to the ω-k diagram defined for the solar acoustic and gravity modes.) The low-latitude ω-k diagram shows ridges which mark different radial orders of the inertial modes. The positions of the ridges are found to be very sensitive to the depth of the convection zone and the slope of the rotation profile within the convection zone.

Changing the depth of the convection zone changes the spacing between the ridges in the ω-k diagram, and changing the rotation profile changes the absolute frequency positions of ridges, shifting them, as a whole, down or up in frequency. Because the two effects are independent, one can determine both the convection zone depth and the rotation profile from a low-latitude ω-k diagram constructed from observations of inertial oscillations.

Solar inertial modes have not been observed. The 2 week to 1 month periods of the modes and their low-latitude structure require an observation program of at least 1 year duration and the ability to resolve at least 2° in latitude (at the equator). The Fourier Tachometer, developed jointly by the High Altitude Observatory and the National Solar Observatory under the direction of T. Brown (HAO) and J. Evans (NSO), promises to be able to observe these modes, assuming that the modes are excited to sufficient amplitude (~ 1 m s^{-1}).

In § II we derive the pulsation equations used to describe the axisymmetric inertial oscillations. The equations are written in the form of a modified eigenvalue problem. In § III we describe the solutions of the pulsation equations. We introduce the low-latitude ω-k diagram and show its diagnostic capabilities with respect to the depth and rotation profile of the convection zone. In the final section we summarize the results of this work. We also discuss the feasibility of observing the inertial oscillations with enough resolution to produce a low-latitude ω-k diagram. We conclude the final section with a brief description of our future objectives.

II. EQUATIONS

a) Assumptions

The inertial modes of the Sun have oscillation periods of the order of half a solar rotation period, hence the effects of acoustic modes, with periods shorter than 30 minutes, are neglected. To eliminate these modes, we use the anelastic approximation. This is effected by dropping the $\partial \rho / \partial t$ terms in the general fluid flow equations (Gilman and Glatzmaier 1981, eqs. [1]–[7]). Since the inertial modes are expected to be confined to the adiabatically stratified convection zone, buoyancy terms, which produce gravity modes (periods of the order of 1 hour), are also dropped.

In the first study we investigate only the axisymmetric modes, hence the equations do not carry any longitudinal dependence. We further simplify the problem by describing the convection zone as an adiabatic shell, in hydrostatic equilibrium, composed of fully ionized hydrogen.

The rotation rate of the Sun is low; therefore, centrifugal terms, appearing as the square of the rotation rate, are neglected, and equipotential surfaces are taken to be spherically symmetric. All viscous terms are also neglected.

The rotation rate profile is assumed to be constant along cylinders aligned with the north-south rotation axis, i.e., it is a function of the radius of the cylinder only. In this work we have investigated the family of rotation curves defined by

$$u_0(r, \phi) = r \cos \phi \left[a + b \left(1 - \frac{r^2 \cos^2 \phi}{r_s^2} \right) + c \left(\frac{r^2 \cos^2 \phi}{r_s^2} \right)^2 \right], \tag{1}$$

where u_0 is the unperturbed fluid velocity in the east-west direction; r is the radial position; ϕ is the latitudinal position; a, b, and c are constant terms which define the rotation frequency at the Sun's surface; and r_s is the radius of the surface; c is taken to be identically zero throughout this work. We chose this profile for the following reasons.

1. The rotation profile is easily fitted to the observed surface rotation, described by

$$\Omega(\phi) = a + b \sin^2 \phi + c \sin^4 \phi . \tag{2}$$

2. One family of global convection models (Glatzmaier 1984; Gilman 1984; Gilman and Miller 1985) predicts this profile for the Sun.

3. This profile falls out naturally from the equations describing the rotating reference state (eqs. [31] and [32]).

The boundary conditions at the surface and the base of the convection zone are taken so that the motion is confined to the spherical shell between these two layers. Boundary conditions are also required at the equator because we have numerically solved the resulting equations in a single hemisphere only. To simplify the mathematics, we have chosen these boundary conditions so that the fluid flow associated with the oscillations does not cross the equator. Other symmetries at this boundary will be investigated in future work.

Under the above assumptions the nonlinear fluid equations are linearized and rewritten in the form of a modified eigenvalue problem. The modified eigenvalue problem is then solved numerically for both the eigenvalues (normalized frequencies squared) and the corresponding eigenfunctions.

b) Derivation of Equations

From equations (1), (2), (3), and (7) of Gilman and Glatzmaier (1981), and keeping in mind the above assumptions, we have the following system of equations describing fluid motion in a rotating spherical coordinate system.

For east-west flow we have

$$\rho \frac{\partial u}{\partial t} = \rho \left(2\Omega + \frac{u}{r \cos \phi} \right) \sin \phi v - \rho \left(2\Omega \cos \phi + \frac{u}{r} \right) w - \left[\frac{1}{r \cos \phi} \frac{\partial}{\partial \phi} (\rho uv \cos \phi) + \frac{1}{r^2} \frac{\partial}{\partial r} (\rho uwr^2) \right]. \tag{3}$$

For north-south flow,

$$\rho \frac{\partial v}{\partial t} = -\frac{1}{r} \frac{\partial p}{\partial \phi} - \rho \left(2\Omega + \frac{u}{r \cos \phi} \right) \sin \phi u - \frac{\rho vw}{r} - \left[\frac{1}{r \cos \phi} \frac{\partial}{\partial \phi} (\rho v^2 \cos \phi) + \frac{1}{r^2} \frac{\partial}{\partial r} (\rho r^2 vw) \right]. \tag{4}$$

For radial flow,

$$\rho \frac{\partial w}{\partial t} = -\frac{\partial p}{\partial r} - \rho g + \rho \left(2\Omega \cos \phi + \frac{u}{r} \right) u + \frac{\rho v^2}{r} - \left[\frac{1}{r \cos \phi} \frac{\partial}{\partial \phi} (\rho vw \cos \phi) + \frac{1}{r^2} \frac{\partial}{\partial r} (\rho r^2 w^2) \right]. \tag{5}$$

The mass continuity equation becomes

$$\frac{1}{r^2} \frac{\partial}{\partial r} (r^2 \rho w) + \frac{1}{r \cos \phi} \frac{\partial}{\partial \phi} (\cos \phi \rho v) = 0, \tag{6}$$

and the conservation of energy, expressed in thermodynamic variables, becomes

$$\frac{\partial s}{\partial t} + \frac{v}{r} \frac{\partial s}{\partial \phi} + w \frac{\partial s}{\partial r} = 0. \tag{7}$$

Here u, v, and w are, respectively, the east-west, north-south, and radial velocity components; Ω is the rotation frequency of the reference frame, ϕ is the latitude, r is the radius, ρ is the density, p is the pressure, g is the gravitational acceleration, and s is the specific entropy.

The physical variables of the system are expanded into stationary and perturbed variables, as follows:

$$\rho = \bar{\rho}(r) + \rho_0(r, \phi) + \rho'(r, \phi, t), \tag{8}$$

$$p = \bar{p}(r) + p_0(r, \phi) + p'(r, \phi, t), \tag{9}$$

$$s = \bar{s}(r) + s_0(r, \phi) + s'(r, \phi, t), \tag{10}$$

$$u = u_0(r, \phi) + u'(r, \phi, t), \tag{11}$$

$$v = v'(r, \phi, t), \tag{12}$$

$$w = w'(r, \phi, t). \tag{13}$$

The variables are split into three different scales defined by the ordering $\bar{\rho} \gg \rho_0 \gg \rho'$, $\bar{p} \gg p_0 \gg p'$, etc. The variables $\bar{\rho}(r)$, $\bar{p}(r)$, and $\bar{s}(r)$ define the physical state of the nonrotating, adiabatically stratified shell, and $\rho_0(r, \phi)$, $p_0(r, \phi)$, $s_0(r, \phi)$, and $u_0(r, \phi)$ define the departures of the physical variables from the nonrotating reference state to the reference state which is rotating as defined by equation (1). In particular, u_0 represents the rotation velocity of the fluid. If the rotating shell is perturbed slightly, the fluid is set into motion. The perturbed fluid and its motion are described by the primed variables. Substituting these variables in the fluid flow equations allows the problem to be split into three separate systems of equations: those of the nonrotating reference state, those of rotating reference state, and the oscillation equations.

The presence of the Coriolis force produces oscillation patterns which are related to the usual spherical harmonics (Greenspan 1968). Confining the fluid flow to a spherical shell distorts the oscillation pattern, so much so that the motion can no longer be conveniently described as an expansion in spherical harmonics. Introducing rotation of course breaks the spherical symmetry of the problem. Confining the motion to a shell enhances this effect. Fluid motions in the equatorial regions experience the Coriolis force perpendicular to the gradient in stratification, whereas fluid motion in polar regions experience the Coriolis force parallel to the gradient in stratification. The shallowness of the shell allows the two regions to set up distinct oscillation patterns, independently of each other.

The nonrotating reference state is in hydrostatic equilibrium,

$$\frac{\partial \bar{p}}{\partial r} = -\bar{\rho} g , \tag{14}$$

adiabatically stratified,

$$\frac{1}{\bar{\rho}} \frac{d\bar{\rho}}{dr} = \frac{1}{\gamma \bar{p}} \frac{d\bar{p}}{dr} , \tag{15}$$

and, we shall assume, an ideal gas,

$$\bar{p} = R_* \bar{\rho} \bar{\theta} , \tag{16}$$

where R_* is the gas constant divided by the mean molecular weight and $\bar{\theta}$ is the temperature. We also take

$$g(r) = \frac{g_s r_s^2}{r^2} , \tag{17}$$

where g_s is the gravitational acceleration at the surface ($r = r_s$). Solving for $\bar{p}$, $\bar{\rho}$, and $\bar{\theta}$ as functions of radius in equations (14)–(17), we find that the nonrotating reference state can be defined by

$$\frac{\bar{p}}{p_s} = \left[\frac{\gamma - 1}{\gamma} \frac{g_s r_s}{R_* \theta_s} \left(\frac{r_s}{r} - 1 \right) + 1 \right]^{\gamma/(\gamma - 1)} , \tag{18}$$

$$\frac{\bar{\rho}}{\rho_s} = \left[\frac{\gamma - 1}{\gamma} \frac{g_s r_s}{R_* \theta_s} \left(\frac{r_s}{r} - 1 \right) + 1 \right]^{1/(\gamma - 1)} , \tag{19}$$

$$\frac{\bar{\theta}}{\theta_s} = \left[\frac{\gamma - 1}{\gamma} \frac{g_s r_s}{R_* \theta_s} \left(\frac{r_s}{r} - 1 \right) + 1 \right] . \tag{20}$$

Substituting the variable expressions of equations (8)–(13) in equations (3)–(7) yields, for the rotating reference state,

$$\frac{1}{r} \frac{\partial p_0}{\partial \phi} + 2\bar{\rho} \Omega \sin \phi u_0 = 0 , \tag{21}$$

$$\frac{\partial p_0}{\partial r} + \rho_0 g - 2\bar{\rho} \Omega \cos \phi u_0 = 0 , \tag{22}$$

and

$$s_0 \approx c_v \frac{p_0}{\bar{p}} - c_p \frac{\rho_0}{\bar{\rho}} , \tag{23}$$

where we have assumed $\rho' \ll \rho_0 \ll \bar{\rho}$ and $\bar{s} = 0 = c_v \ln \bar{p} - c_p \ln \bar{\rho}$ (adiabatically stratified layer).

We also obtain from this substitution, to first order in the perturbed variables,

$$\frac{\partial u'}{\partial t} = \frac{-1}{r} \frac{\partial}{\partial \phi} (u_0 v') - \frac{1}{\bar{\rho}} \frac{\partial}{\partial r} (\bar{\rho} u_0 w') + 2\Omega \sin \phi v' - 2\Omega \cos \phi w' - \frac{3u_0 w'}{r} + \frac{2u_0 \sin \phi}{r \cos \phi} v' , \tag{24}$$

$$\frac{\partial v'}{\partial t} = \frac{-1}{r} \frac{\partial \Pi'}{\partial \phi} - 2\Omega \sin \phi u' - \frac{2 \sin \phi u_0 u'}{r \cos \phi} , \tag{25}$$

$$\frac{\partial w'}{\partial t} = -\frac{\partial \Pi'}{\partial r} + \frac{s' g}{c_p} + 2\Omega \cos \phi u' + \frac{2u_0 u'}{r} , \tag{26}$$

$$\frac{\partial s'}{\partial t} + \frac{v'}{r} \frac{\partial s_0}{\partial \phi} + w' \frac{\partial s_0}{\partial r} = 0 , \tag{27}$$

and

$$\frac{1}{r^2} \frac{\partial}{\partial r} (r^2 \bar{\rho} w') + \frac{1}{r \cos \phi} \frac{\partial}{\partial \phi} (\cos \phi \bar{\rho} v') = 0 , \tag{28}$$

where

$$\Pi' = \frac{p'}{\bar{\rho}} . \tag{29}$$

Defining

$$\Pi_0 = \frac{p_0}{\bar{\rho}} , \tag{30}$$

and setting $s_0 = 0$, the rotating reference state is completely described by

$$\frac{1}{r} \frac{\partial \Pi_0}{\partial \phi} + 2\Omega \sin \phi u_0 = 0 , \tag{31}$$

$$\frac{\partial \Pi_0}{\partial r} - 2\Omega \cos \phi u_0 = 0 , \tag{32}$$

and equation (1), the assumed rotation profile. Note that the rotation profile defined in equation (1) is a solution of this system.

Having set $s_0 = 0$, the perturbed motion is now described by equations (24), (25), (28), and

$$\frac{\partial w'}{\partial t} = \frac{-\partial \Pi'}{\partial r} + 2\Omega \cos \phi u' + \frac{2u_0 u'}{r} . \tag{33}$$

Equation (27) drops out.

We introduce the stream function, ψ, defined such that

$$w' = -\frac{1}{\bar{\rho} r^2 \cos \phi} \frac{\partial \psi}{\partial \phi} \tag{34}$$

and

$$v' = \frac{1}{\bar{\rho} r \cos \phi} \frac{\partial \psi}{\partial r} . \tag{35}$$

Rewriting the perturbed motion equations in terms of the stream function yields

$$\frac{\partial u'}{\partial t} = \left(\frac{2\Omega \sin \phi}{\bar{\rho} r \cos \phi} - \frac{1}{r^2 \bar{\rho} \cos \phi} \frac{\partial u_0}{\partial \phi} + \frac{u_0 \sin \phi}{\bar{\rho} r^2 \cos^2 \phi} \right) \frac{\partial \psi}{\partial r} + \left(\frac{2\Omega}{r^2 \bar{\rho}} + \frac{1}{r^2 \bar{\rho} \cos \phi} \frac{\partial u_0}{\partial r} + \frac{u_0}{\bar{\rho} r^3 \cos \phi} \right) \frac{\partial \psi}{\partial \phi} , \tag{36}$$

$$\frac{\partial}{\partial t} \left[\frac{\partial}{\partial r} \left(\frac{1}{\bar{\rho} \cos \phi} \frac{\partial \psi}{\partial r} \right) + \frac{\partial}{\partial \phi} \left(\frac{1}{\bar{\rho} r^2 \cos \phi} \frac{\partial \psi}{\partial \phi} \right) \right] = -2\Omega r \sin \phi \frac{\partial u'}{\partial r} - 2\Omega \cos \phi \frac{\partial u'}{\partial \phi} - \frac{2 \sin \phi}{\cos \phi} \frac{\partial}{\partial r} (u_0 u') - \frac{2}{r} \frac{\partial}{\partial \phi} (u_0 u') . \tag{37}$$

Equation (28) is automatically satisfied. Equation (37) was obtained by cross-differentiating and summing equations (33) and (25) to eliminate Π'.

c) The Modified Eigenvalue Problem

Equations (36) and (37) can be solved numerically as a modified eigenvalue problem. The details of this step are described in Appendix A. Here we will describe this approach only in general terms.

We eliminate the time dependence in equations (36) and (37) by taking

$$\psi \to \psi \exp (i2\Omega\lambda t) \tag{38}$$

and

$$u' \to u' \exp (i2\Omega\lambda t) , \tag{39}$$

in which λ is therefore the dimensionless frequency. In plots involving frequency, we will use the variable $\omega = 2\lambda$. With the following normalization, where D is the convection zone depth,

$$u' = D\Omega U , \qquad u_0 = D\Omega U_0 , \tag{40}$$

$$\psi = \rho_s D^3 \Omega \Psi , \tag{41}$$

$$\hat{\rho} = \bar{\rho}/\rho_s , \tag{42}$$

equations (36) and (37) become

$$i\lambda U = \left[-\left(\frac{\sin \phi}{\hat{\rho} \xi \cos \phi} - \frac{1}{2\xi^2 \hat{\rho} \cos \phi} \frac{\partial U_0}{\partial \phi} + \frac{\sin \phi}{2\xi^2 \hat{\rho} \cos^2 \phi} U_0 \right) \frac{\partial}{\partial x} + \left(\frac{1}{\hat{\rho} \xi^2} - \frac{1}{2\xi^2 \hat{\rho} \cos \phi} \frac{\partial U_0}{\partial x} + \frac{1}{2\xi^3 \hat{\rho} \cos \phi} U_0 \right) \frac{\partial}{\partial \phi} \right] \Psi , \tag{43}$$

$$i\lambda \left(\frac{1}{\hat{\rho} \cos \phi} \frac{\partial^2}{\partial x^2} + \frac{1}{\hat{\rho} \xi^2 \cos \phi} \frac{\partial^2}{\partial \phi^2} - \frac{1}{\hat{\rho}^2 \cos \phi} \frac{d\hat{\rho}}{dx} \frac{\partial}{\partial x} + \frac{\sin \phi}{\hat{\rho} \xi^2 \cos^2 \phi} \frac{\partial}{\partial \phi} \right) \Psi$$

$$= \left[\left(\xi \sin \phi + \frac{U_0 \sin \phi}{\cos \phi} \right) \frac{\partial}{\partial x} + \left(-\cos \phi - \frac{U_0}{\xi} \right) \frac{\partial}{\partial \phi} + \left(\frac{\sin \phi}{\cos \phi} \frac{\partial U_0}{\partial x} - \frac{1}{\xi} \frac{\partial U_0}{\partial \phi} \right) \right] U , \tag{44}$$

where $x \equiv (r_s - r)/D$ and $\xi \equiv r_s/D - x$.

Rewriting equations (43) and (44) in operator form, we have

$$i\lambda U = \mathscr{F}(\Psi) \,, \tag{45}$$

and

$$i\lambda \mathscr{G}(\Psi) = \mathscr{H}(U) \,, \tag{46}$$

where $\mathscr{F}$, $\mathscr{G}$, and $\mathscr{H}$ are linear differential operators. Equations (45) and (46) are in the form of a modified eigenvalue problem distinguished by the operator $\mathscr{G}$ on the left-hand side of equation (46). Combining the two equations shows that the problem reduces to a single-eigenvalue problem:

$$-\mathscr{F}(\mathscr{G}^{-1}(\mathscr{H}(U))) = \lambda^2 U \,, \tag{47}$$

or

$$-\mathscr{G}^{-1}(\mathscr{H}(\mathscr{F}(\Psi))) = \lambda^2 \Psi \,. \tag{48}$$

With the use of finite-difference methods to represent the linear differential operators, either of the previous two equations can be solved as an algebraic eigenvalue problem.

We have chosen, at this time, boundary conditions which confine the fluid flow to one quadrant, i.e., $\Psi(x, \phi) = 0$ on the boundaries (surface and base of convection zone, north pole axis, and equatorial plane). The outer surface was taken to be at 95% of the solar radius, consistent with the assumption of an adiabatic stratification, and to improve convergence of the solutions in this first study. This completes the derivation of the equations.

III. THE SOLUTIONS

a) The Method

The finite-difference equations, corresponding to the modified eigenvalue form of the fluid flow equations, were solved for the stream functions on a staggered grid (see Appendix A). The grid resolution is 19 points in radius, from the base to the top of the shell, and 43 points in latitude, from the equator to the pole. Higher resolutions would have required more computer memory than was conveniently available. The program uses about eight megabytes of memory and takes approximately 1600 minutes of VAX 11-750 central processing time to run, generating 817 eigenvalues and corresponding eigenfunctions, occupying 20 megabytes of file space. For most of the runs only the first 200 eigenfunctions, corresponding to the 200 highest frequency modes, were calculated, thereby reducing the amount of output (CPU time was not significantly reduced). The U-velocities were calculated from the stream functions using the finite-difference form of equation (45).

Between 5% and 20% of the highest frequency modes are complex (occurring in conjugate pairs). The number of complex eigenvalues is a function of the amount of differential rotation assumed: the number of complex eigenvalues among the first 200 modes decreases as b is reduced from 0.00 to -0.30. The magnitude of the imaginary part of the complex eigenvalue does not change when coarser grids are used but remains at about 0.001 times the real part. At this time we cannot explain the complex eigenvalues other than to guess that they are an artifact of the numerical method and may represent truncation errors. For solid-body rotation ($b = 0.0$), the imaginary part cannot represent the growth rate for a physical instability, since there is no available energy in the reference state.

It should be noted that the order in which the eigenvalues are generated by the eigenvalue solving program is not preserved between runs with different differential rotation curves or different convection zone depths.

The contour plots that are described in this section are obtained directly from the eigenfunctions (stream functions) generated from the eigenvalue solving program. The amplitudes of the stream functions and the U-velocities have not been normalized. Since the calculation is linear, the amplitudes of different eigenfunctions cannot be used to infer the relative strengths of the eigenfunctions.

b) General Results

The contour plots of the stream functions and the U-velocities reveal some of the general characteristics of the modes. The modes can exhibit very complex structure. For example, Figure 1 gives stream functions for three different solutions for a uniformly rotating reference state. Notice that in Figure 1a the radial order of the oscillation mode is different at the equator than in the latitude region 15°–30°. It is therefore readily apparent that the usual spherical harmonic classification scheme cannot conveniently be used to classify these modes, although a spherical harmonic expansion can still be used to solve the equations. We will therefore use the word "order" with either the adjective "radial" or "latitudinal" to describe the structure of the mode, in a specific region of the convective shell. The structure of about 5% of the modes is unresolved and beyond classification by any scheme. The number of unresolved modes increases with decreasing frequency.

We can also see that, for a given mode, the largest amplitudes occur either at the equator (Fig. 1a) or at the poles (Fig. 1c) or at the midlatitude (Fig. 1b), but rarely in two or all three of these regions. Clement (1981) alluded to this in his investigations of the low-order axisymmetric inertial modes. Also noted by Clement is the fact that the peak amplitudes of the stream functions and U-velocities remain relatively constant with respect to radius at a given latitude. This is also seen in the contour plots presented here, although the peak amplitudes do decrease slightly with increasing depth (see Fig. 3c, for example).

It is easy to demonstrate that in each mode the stream functions and U-velocities should be spatially out of phase by one-quarter wavelength. This property is verified in Figure 2. Figure 2a shows the stream function for a well-resolved low-order mode, and Figure 2b shows the U-velocities for the same mode. This is a general characteristic of all of the modes calculated.
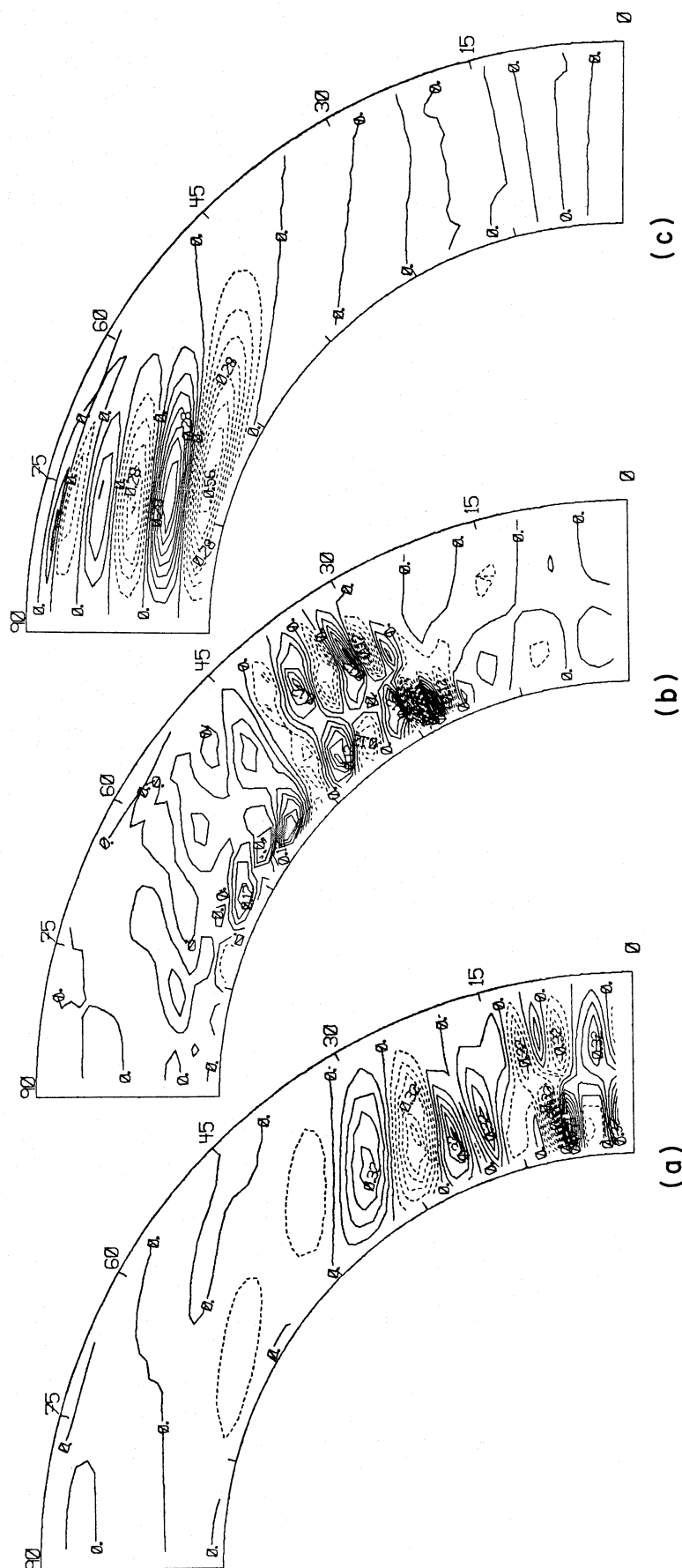
FIG. 1.—Contour plot of several typical stream functions for $b = 0.0$ (solid-body rotation) and (a) $\omega = 1.841\,\Omega_\odot$, ($b$) $1.6363\,\Omega_\odot$, and (c) $1.9271\,\Omega_\odot$. The convection zone depth is 2×10^{10} cm, illustrating modes with peak amplitudes in low, middle, and high latitudes.
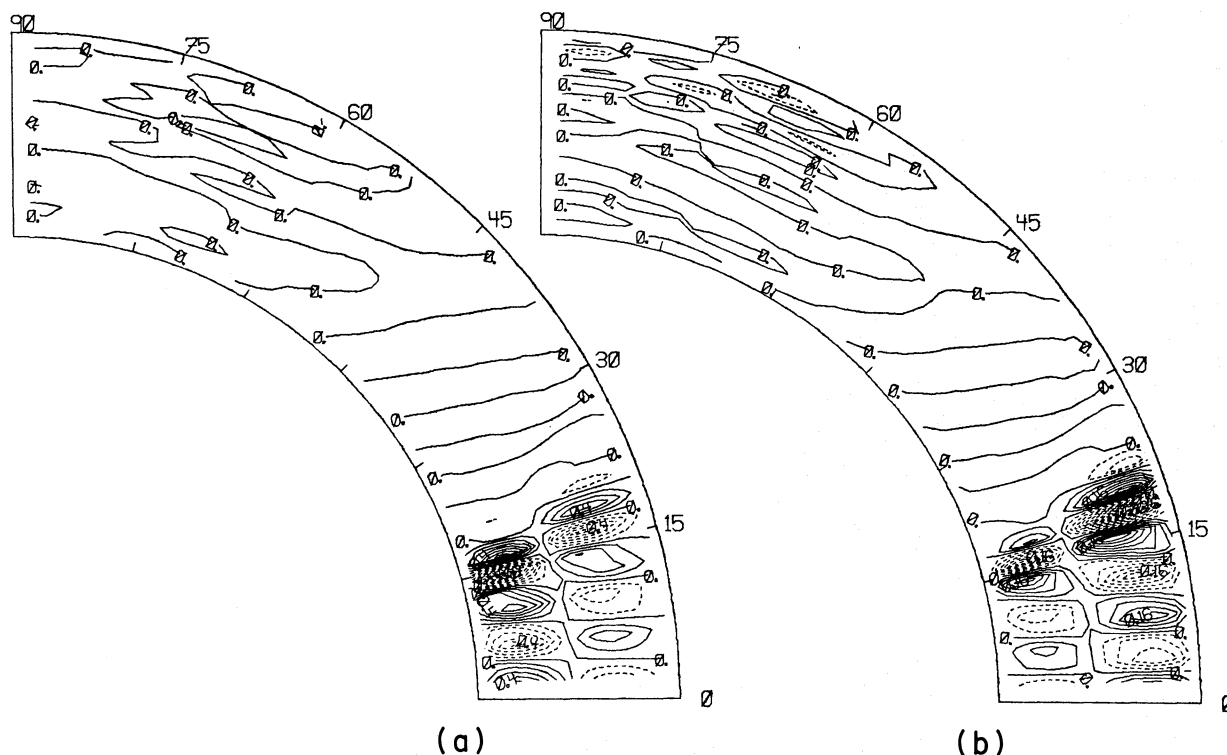
(a)   (b)

Fig. 2.—Contour plot of stream function (a) and U-velocity (b) for the same mode; $b = 0.0$ and $\omega = 1.7966 \ \Omega_\odot$

Most of the modes show recognizable circulation patterns near the equator. Figures 3a–3d illustrate, first, second, third, and fourth radial order modes that have distinctly different frequencies. We later show that these modes fall on distinct nodal lines in a low-latitude ω-k diagram. In Paper II we describe a one-dimensional model of the equatorial region, where most of the well-defined structure exists. The model facilitates the detailed interpretation of many of the characteristics of the modes described in this paper.

Clement (1981, 1984) describes frequency ranges where the spectra of modes become very dense, possibly continuous. Since we are solving an eigenvalue problem on a grid of 19 × 43 elements, we get 817 discrete eigenvalues regardless of the nature of the frequency spectrum. We do, however, see many sequences of eigenvalues and eigenfunctions which have very nearly the same frequency and only slightly different spatial structures. An example is provided in Figures 4c, 5a, and 5b. Eigenfunctions in the sequences have the same radial and latitudinal order but are spatially shifted slightly with respect to each other. The complex eigenvalues also appear in sequences, with the real part remaining the same and the complex part changing. We do not know whether these features are related to the dense or continuous frequency ranges described by Clement.

c) Depth and Differential Rotation Dependence

The modified eigenvalue equations were solved for two different convection zone depths and four different rotation curve profiles (see Table 1). The depths chosen bracket solar convection zone depths calculated from theory and inferred from observations. The standard solar models calculated from stellar evolution programs favor shallower depths, while observational results, such as the 5 minute oscillation spectrum and the surface abundances of lithium and beryllium, are best interpreted with a deeper convection zone. The discrepancy between theory and observation has not been resolved, although there is evidence that mixing may extend beneath the base of the convection zone by some form of a convective overshooting mechanism (Gough 1984).

The differential rotation on the surface of the Sun corresponds to $b = -0.30$ in equation (2), that is to say, the rotation frequency of the Sun is 0.3 less at the poles than at the equator. When $b = 0$ ($c = 0$ and $a = 1$), the convective shell is in solid-body rotation. A negative b corresponds to a rotation rate which is decreasing with depth, and, conversely, a positive b corresponds to a rotation rate which is increasing with depth. In all cases the rotation rate at the surface at the equator is assumed to be the same, i.e., unity, the normalized solar equatorial rotation rate.

Because the eigenvalue solving program does not order the modes consistently between different runs, and because some of the modes are false (artifacts of the grid resolution), it is difficult to identify a given mode through changes in the rotation rate profile. Figures 4a, 4b, and 4c follow one of the most distinct modes through from $b = 0.00$ to $b = -0.30$. (Note: the mode does not appear at $b = 0.15$.) Other modes can be traced in a similar manner, but this mode is the most easily followed.

It is clear that departures from solid-body rotation complicate the structure of the mode, adding structure on a decreasing length scale as the absolute value of the change in rotation frequency is increased. The frequencies decrease as the value of b decreases. This can be understood in terms of the average restoring force, the Coriolis force, which the mode experiences within the spherical shell. Decreasing the rotation rate with depth, negative b, decreases the strength, at a given depth, of the Coriolis force with respect to the solid-body case. The restoring force, then, is on average less in the negative b models, hence the frequency of the oscillation
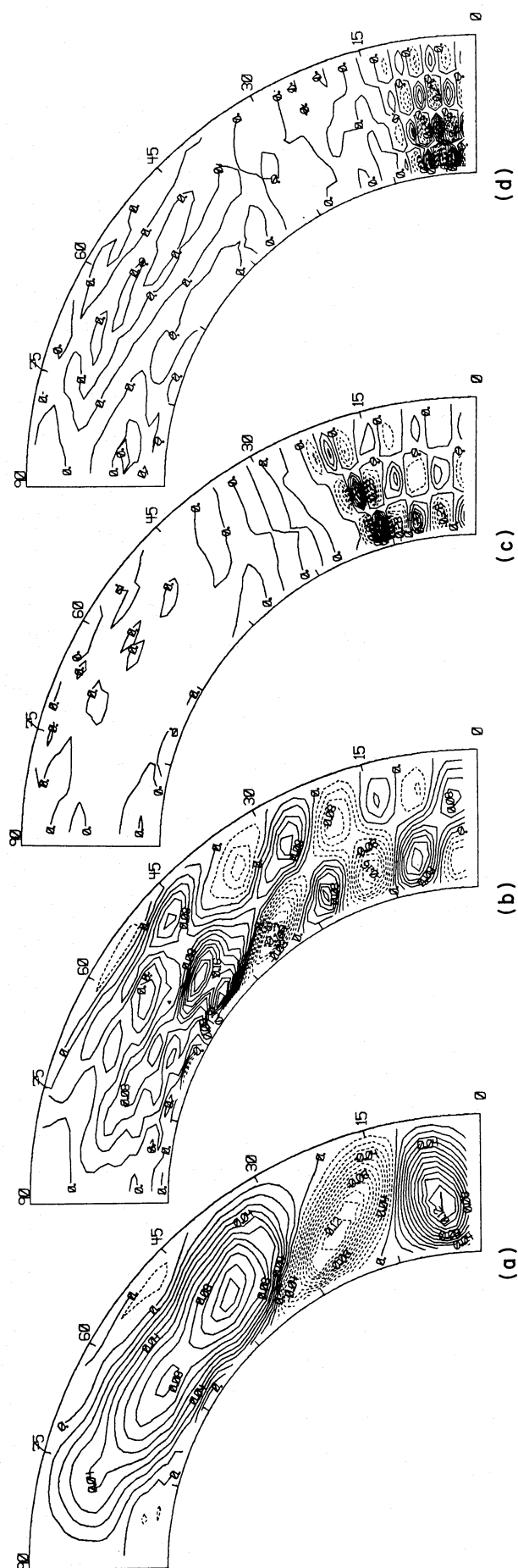
FIG. 3.—Examples of first, second, third, and fourth radial order stream functions $b = 0.0$ and (a) $\omega = 1.6234\,\Omega_\odot$, (b) $1.6503\,\Omega_\odot$, (c) $1.6564\,\Omega_\odot$, and (d) $1.5938\,\Omega_\odot$

FIG. 4.—Contour plots of the same stream function in convection zones with different rotation profiles. They are (a) b = 0.0, (b) b = 0.15 and (c) b = 0.30. The corresponding frequencies are ω = 1.5141 Ω_⊙, ω = 1.4024 Ω_⊙, and ω = 1.2921 Ω_⊙, respectively.

FIG. 5.—Contour plots of the same stream function shown in Fig. 4. The stream functions in Figs. 5a and 5b, with $\omega = 1.2970\,\Omega_\odot$ and $\omega = 1.2927\,\Omega_\odot$, respectively, and $b = -0.30$, form a triplet along with the stream function in Fig. 4. The convection zone in Fig. 5c has $b = 0.0$ and a depth of 1.5×10^{10} cm. The stream function frequency is $\omega = 1.4803\,\Omega_\odot$.

TABLE 1

SUMMARY OF COMPUTER RUNS

Run Number	Convection Zone Depth (cm)	Differential Rotation Parameter b
1	2.0E10	0.00
2	2.0E10	−0.30
3	2.0E10	−0.15
4	2.0E10	0.15
5	1.5E10	0.00
6	1.5E10	−0.15

decreases. The actual strength of the restoring force does not depend only on the Coriolis force, but includes terms related to the angular momentum. This is explained in Paper II, where the simplified one-dimensional model is easier to interpret in this respect.

When a well-defined mode is followed through the different values of b, the mode may disappear for a specific b-value, or it may split into several modes of nearly the same frequency. For example, the single mode at $b = 0.00$ (Fig. 4a) splits into the three modes shown in Figures 4c, 5a, and 5b, at $b = −0.30$. At this time we cannot track these changes clearly because of the limited number of b-values used. In future work we will fill in the gaps in b, and trace out in detail the spatial changes of several modes as b is varied.

Decreasing the depth of the shell from $D = 2.0 \times 10^{10}$ cm to $D = 1.5 \times 10^{10}$ cm does not affect the general features of the modes. The shell is narrower, however, and some of the larger scale modes are perturbed. For example, the mode corresponding to Figures 4a–4c is shown in Figure 5c.[3]

Figures 6a and 6b compare two modes of nearly the same radial and latitudinal wavelengths, in the equatorial regions. Even though the two modes exist in shells which have different depths, they have almost the same frequency. In the next subsection we will show this to be a general characteristic of all of the modes.

d) Low-Latitude ω-k Diagram

For many of the modes, the largest amplitudes of oscillation are found near the equator, hence the frequencies of these modes are determined primarily by the structure near the equator. Using this property, a frequency (ω) versus low-latitude wavenumber (k) diagram was constructed. The diagram immediately brought order to the thousands of eigenvalues and eigenfunctions calculated.

[3] The matching of similar modes in shells which have different depths or different rotation profiles is subjective. The modes that are identified here have low-order structure which stands out among the more complicated structures or their neighboring modes.
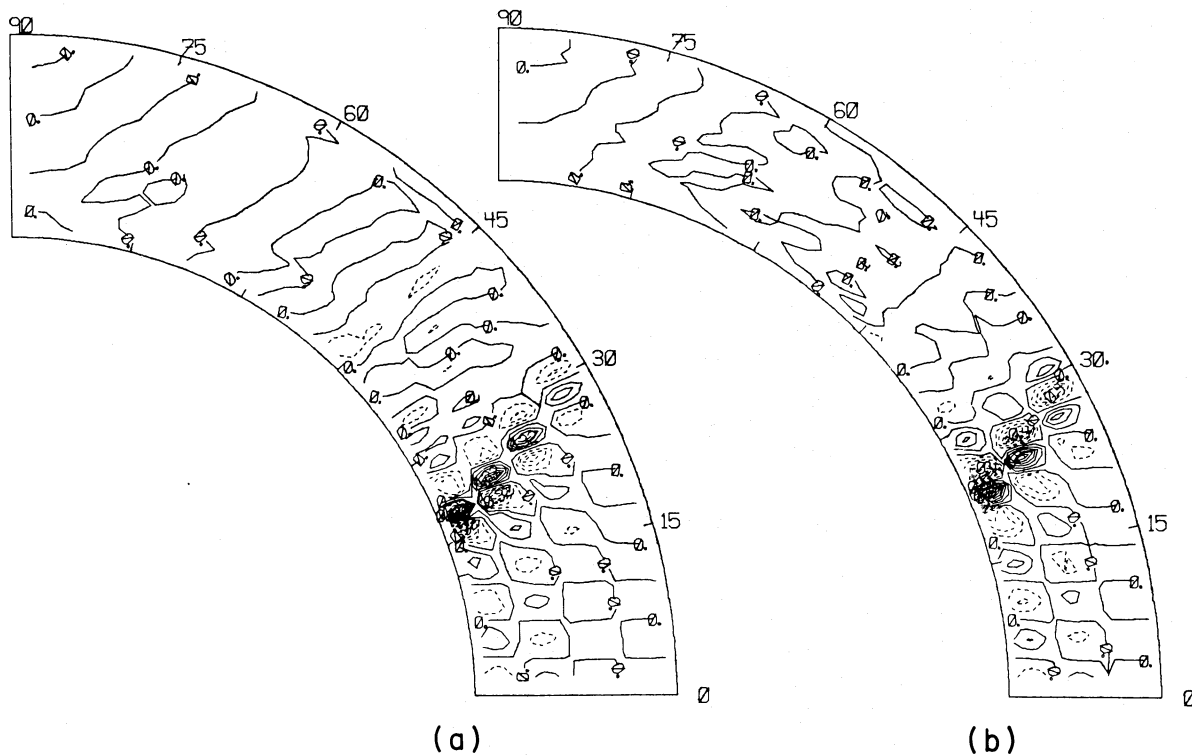

(a)   (b)

FIG. 6.—Stream functions of (a) a fourth radial order mode, $\omega = 1.4543\,\Omega_\odot$ and (b) a third radial order mode, $\omega = 1.4646\,\Omega_\odot$. The convection zone depths are 2.0×10^{10} cm and 1.5×10^{10} cm, respectively ($b = 0.0$).

The number of nodes between $0°$ and $15°$ latitude was counted and then converted to the average latitudinal wavenumber, by

$$k = \frac{360°}{15°} \frac{1}{2}\left(n_u - \frac{1}{2}\right),$$ (49)

where k is the wavenumber in units of $2\pi/R_\odot$ and n_u is the node number. For example, the node in Figure 2b has a frequency $\omega = 1.7966 \, \Omega_\odot$, where $\Omega_\odot$ is the Sun's equatorial rotation frequency, and a node number $n_u = 4.7$ nodes, between the equator and $15°$ latitude. The nodes were counted on the U-velocity contours because this is the velocity component which would be most readily observed. In most cases it was easy to estimate the node number within ± 0.1 node.

Figures 7a–7d show ω-k diagrams for a convection zone whose depth is 2.0×10^{10} cm, and Figures 7e and 7f show ω-k diagrams for a shallower convection zone (1.5×10^{10} cm). The data separate into ridges. The ridges correspond to the radial order (at the equator) of the modes. The ridges from right to left denote first, second, third, etc., radial order modes.

Two major characteristics common to all of the ω-k diagrams shown are immediately apparent. First, for a given radial order, the modes of smaller latitudinal scale (high node number) have higher frequency. Second, higher radial orders for a given latitudinal scale have lower frequencies. These features can be understood when one remembers that the Coriolis force acts only in the plane perpendicular to the rotation axis. Fluid elements displaced in latitude near the equator feel no Coriolis force in that direction. Mode patterns shortened in latitude compared with radial extent will contain mostly radial, as well as longitudinal, displacements, and therefore higher average acceleration from the Coriolis force, leading to a higher frequency. Fluid in mode patterns elongated in latitude compared with their radial extent experience much less acceleration on average, and therefore are associated with lower frequencies.

The above argument should imply that all the radial orders should approach the same frequency (2Ω) asymptotically at extremely high latitude node number. Figure 7 gives only a hint of this behavior, but this result is demonstrated for the cylindrical problem in Paper II.

With respect to changes in the rotation rate (compare Figs. 7a–7d, for example), it is clear that decreasing the frequency of rotation with depth (negative b) decreases the frequency of the modes, and vice versa. This is true for both convection zone depths. As has already been explained, this behavior can be understood in terms of the strength of the average Coriolis force in the spherical shell, which decreases with decreasing b. The Coriolis force is the principal restoring force.

Comparing Figure 7c with Figures 7e, and Figure 7d with Figure 7f, one sees that decreasing the depth of the convection zone spreads the ridges apart. To understand this behavior, recall the example in the previous subsection, where the frequency of a third radial order mode in the shallow convective shell was compared with the frequency of a fourth radial order mode, of identical latitudinal wavenumber, in the deeper convective shell. The frequencies are nearly the same. This is because the mode patterns contain nearly the same proportions of radial and latitudinal displacements. The deeper layer simply has one more layer of circulation cells at the bottom. Overlaying Figure 7c on Figure 7e, for example, will show that the third-order ridge in the ω-k diagram for the shallow convection zone coincides with the fourth-order ridge in the ω-k diagram for the deeper convection zone. The other ridges are displaced proportionally. The ratio of the shell depths, $3:4$, determines the ratio of the relative spacings between the ridges of the modes in the ω-k diagrams for the two shells, $3:4$.

Overlaying Figure 7c on Figure 7e also reveals that for a given latitudinal node number, the lowest radial order frequency is higher for the deeper layer. This is because the lowest radial order mode in the deeper layer has a higher fraction of fluid elements being displaced radially, so more acceleration and therefore a higher frequency result.

It is important to note that the effects of different rotation profiles and different depths on the positions of the ridges in the low-latitude ω-k diagram are independent. Therefore, from a single low-latitude ω-k diagram of these modes one can determine both the depth of the convection zone and its rotation profile. This assumes that the frequencies of the modes are insensitive to the boundary conditions, a point which is especially critical at the base of the convection zone and at the top where the rigid boundary conditions used here are an oversimplification of the truth.

The data reduction error of ± 0.1 node does not account for all of the scatter in the low-latitude ω-k diagrams, especially at the lower frequencies. Some of the scatter is produced by families (sequences) of modes which have similar low-latitude spatial structure but slightly different structure at higher latitudes. The higher latitude structure is not directly accounted for in the low-latitude node counts. The string of modes at $n_u = 5$, $\omega > 2 \, \Omega_\odot$ in Figure 7a, are all associated with large-amplitude structure in the high latitudes.

It is clear that the inertial modes as interpreted through the low-latitude ω-k diagram could be a useful tool to investigate the depth and rotation profile of the solar convection zone, if they can be observed. To resolve the ridges in the low-latitude diagram, it will be necessary to collect oscillation data for at least one year (not necessarily every day) and to be able to resolve $1°$–$2°$ in latitude. If the modes exist and have sufficient amplitudes (the linear calculation presented in this work does not predict amplitudes of the velocities), the Fourier Tachometer, developed jointly by T. Brown and J. Evans at the High Altitude Observatory, Boulder, and the National Solar Observatory, Sunspot, could be used to observe these modes.

IV. SUMMARY AND CONCLUSIONS

The fluid flow equations, describing axisymmetric inertial oscillations in the convective envelope of the Sun, were first written in the form of a modified eigenvalue problem and then solved numerically. The eigensolutions of the modified eigenvalue problem, which correspond to the stream functions of the fluid flow, were obtained on a 19 (radius) × 43 (latitude) resolution grid. U-velocities (longitudinal flow) were calculated directly from the stream functions. Contour plots of the stream functions and U-velocities were constructed and then analyzed.

We find that, although the contour plots show the flow pattern very clearly, the spatial structure of the oscillations cannot easily be classified. The usual method of classifying the modes in terms of spherical harmonics fails because the modes are confined to a
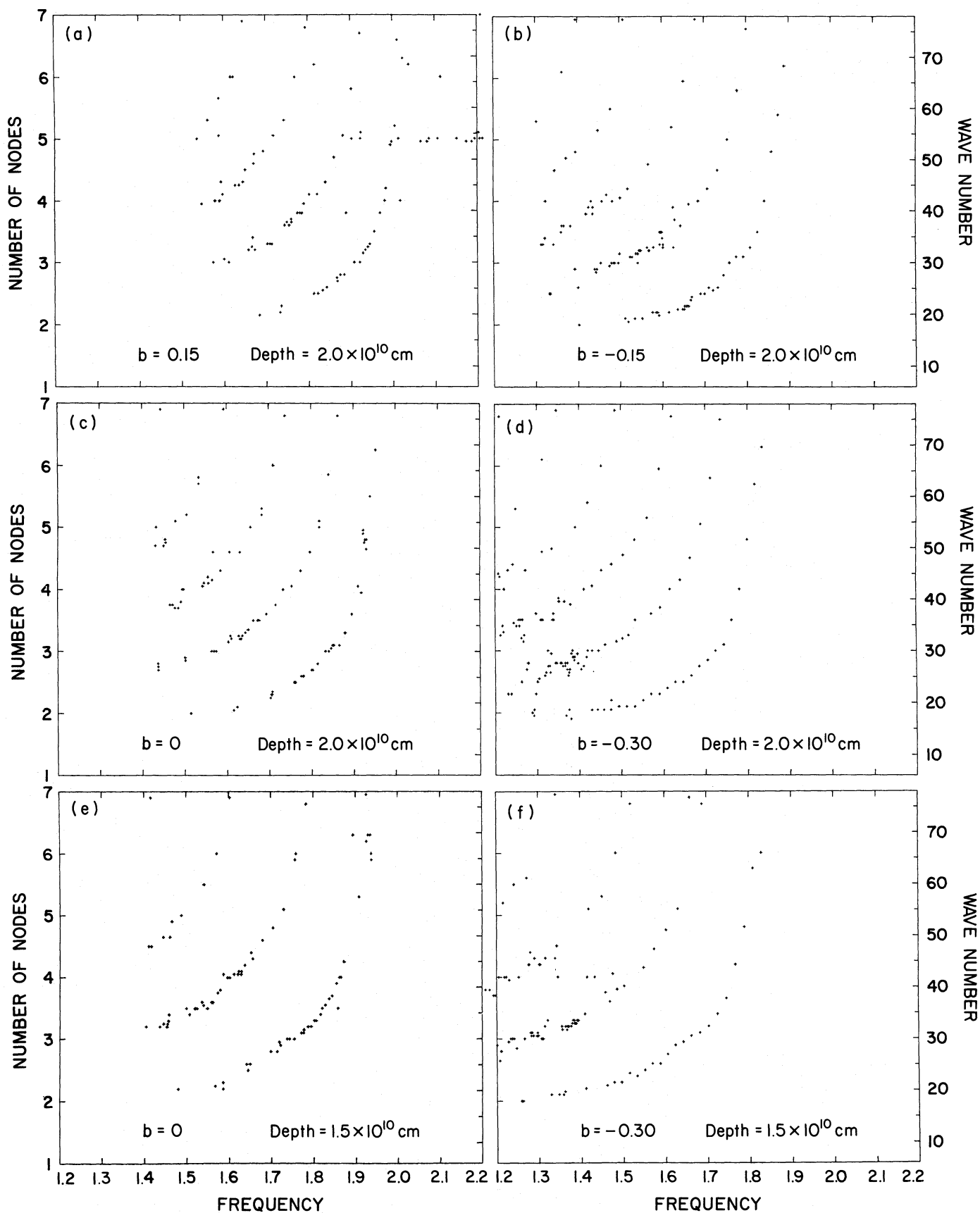
FIG. 7.—(a–f) ω-k diagrams for several combinations of convection zone depth and rotation profiles (see text)

shell. In addition, many modes exhibit different orders of spatial structure at different latitudes. Noticing that many of the more orderly flow patterns are confined to the region $\pm 15°$ of the equator, we constructed a diagram plotting frequency ω against average latitudinal wavenumber k near the equator for this region. The low-latitude ω-k diagram very clearly shows ridge structure. The ridges correspond to modes which have the same radial order, with the highest frequency ridge corresponding to those modes which have zero nodes between the surface and base of the shell, the second highest frequency ridge to those modes with one node, etc.

Low-latitude ω-k diagrams were constructed for several combinations of convective shell depths and rotation profiles. The ridge structure is very sensitive to both. Taking solid-body rotation as a reference, a rotation profile which decreases with depth shifts the ridges toward lower frequencies, and a rotation profile which increases with depth shifts the ridges toward higher frequencies. This can be understood in terms of the average restoring force a fluid element experiences within the convective shell. The restoring force for inertial oscillations is the Coriolis force. The average Coriolis force in a convective shell which has a rotation profile that decreases with depth is less than the average Coriolis force in a convective shell which is rotating as a solid body. The frequencies are lower, in the former case, because the restoring force is less. This argument oversimplifies the true picture. We discuss the dependence of the ridge positions on different rotating profiles in more detail in Paper II. In Paper II we use a cylindrical coordinate system to model the structural behavior of the modes near the equator. The one-dimensional equations of this model are more easily interpreted than the more detailed two-dimensional equations presented here.

The frequency spacing between the ridges is determined by the depth of the convective shell. The ridges are closer together for deeper shells than they are for shallower shells. This is explained fully in § III*d*. It is important to note that dependencies of the ridges on shell depth and rotation profile are different and therefore separable.

Our results indicate that, if solar inertial oscillations can be observed, they will provide a good measure of the convection zone depth as well as the rotation profile within the convection zone.

To resolve the ridge structure in the low-latitude ω-k diagram it will be necessary to undertake a program of observation of at least one year's duration, on an instrument which has a spatial resolution of 2° in latitude, at the equator. The Fourier Tachometer (T. Brown 1984, private communication), located at the National Solar Observatory, Sunspot, New Mexico (developed jointly by the National Solar Observatory and the High Altitude Observatory, Boulder, Colorado), appears capable of such a program. It has a resolution of 1° in latitude near the solar equator. The rms velocity sensitivy of the instrument is primarily determined by supergranulation noise. Taking the supergranule rms velocity to be 300 m s^{-1} and assuming that 200 days of data can be collected (not unreasonable for a one year program), one can expect the lower velocity threshold to be less than 1 m s^{-1} (50 cm s^{-1} at 1 σ). At present we do not know what the surface velocities of the solar inertial oscillations will be. An observation program to observe solar inertial oscillations, using the Fourier Tachometer, has been proposed, tentatively to begin in the fall of 1985.

We were not able to follow the changes in the structure of the inertial oscillations as the rotation profiles were changed because of the limited number of runs made. In future work we will make finer changes between different rotation profiles, so that we can study the crossing, combining, and splitting of modes in more detail. We will also look at more realistic boundary conditions at the base of the convection zone and will generalize the problem to include nonaxisymmetric modes. Because the one-dimensional model used in Paper II is much easier to modify and interpret, many of the more complicated changes to boundary conditions (for example, matching solutions to an inner shell) will first be attempted with this model. Of course, if solar inertial oscillation modes are detected, then the results of the observations will determine the direction of any further work.

APPENDIX

I. FINITE-DIFFERENCE EQUATIONS

Equations (43) and (44) were defined on a staggered grid (see Fig. 8). Although the staggered grid increases the complexity of the program, it has the advantage of doubling the effective resolution of the grid. As seen in Figure 8, the stream functions are defined at the grid line intersections and the U-velocities at the points in between.

We introduce the following notational simplifications:

$$x^+ \equiv x + (dx/2) , \tag{A1}$$

$$x^- \equiv x - (dx/2) , \tag{A2}$$

$$\phi^+ \equiv \phi + (d\phi/2) , \tag{A3}$$

$$\phi^- \equiv \phi - (d\phi/2) , \tag{A4}$$

where dx and $d\phi$ define the grid point spacing in the x- and ϕ-directions.

The finite-difference expressions for the first-order derivatives take their usual form, for example,

$$\frac{\partial u}{\partial x}(x, \phi) = \frac{1}{dx}\left[U(x^+, \phi) - U(x^-, \phi)\right] . \tag{A5}$$

Higher order derivatives are obtained by repeated application of equation (A5). Where it is necessary to evaluate Ψ or U at a point not located at one of their respective grid array points, linear averaging is used to obtain an approximate value at the desired location.
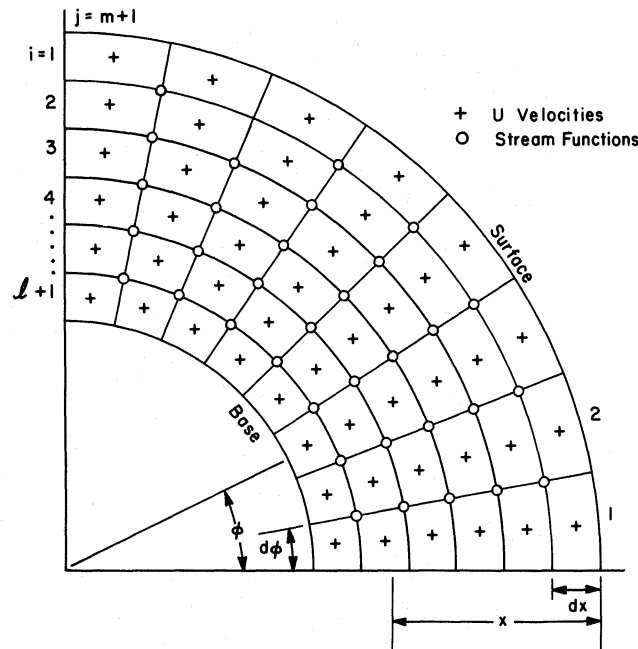
FIG. 8.—Grid layout on which the finite-difference equations for the modified eigenvalue problem are defined

The finite-difference form of equation (43) is

$$i\lambda U(x, \phi) = \Psi(x^+, \phi^+)\left(\frac{a_1}{2dx} + \frac{a_3}{2d\phi}\right) + \Psi(x^-, \phi^+)\left(\frac{-a_1}{2dx} + \frac{a_4}{2d\phi}\right) + \Psi(x^+, \phi^-)\left(\frac{a_2}{2dx} - \frac{a_3}{2d\phi}\right) + \Psi(x^-, \phi^-)\left(\frac{-a_2}{2dx} - \frac{a_4}{2d\phi}\right).$$

(A6)

The a_i will be defined shortly. The finite-difference form of equation (44) is

$$i\lambda\left[\Psi(x^{++}, \phi)\left(\frac{b_1}{dx^2} + \frac{b_3}{2dx}\right) + \Psi(x^{--}, \phi)\left(\frac{b_1}{dx^2} - \frac{b_4}{2dx}\right) + \Psi(x, \phi^{++})\left(\frac{b_2}{d\phi^2} + \frac{b_5}{2d\phi}\right)\right.$$

$$\left. + \Psi(x, \phi^{--})\left(\frac{b_2}{d\phi^2} - \frac{b_6}{2d\phi}\right) + \Psi(x, \phi)\left(\frac{-2b_1}{dx^2} - \frac{2b_2}{d\phi^2} + \frac{b_4 - b_3}{2dx} + \frac{b_6 - b_5}{2d\phi}\right)\right]$$

$$= U(x^+, \phi^+)\left(\frac{c_1}{2dx} + \frac{c_3}{2d\phi} + \frac{c_5}{4}\right) + U(x^-, \phi^+)\left(\frac{-c_1}{2dx} + \frac{c_4}{2d\phi} + \frac{c_6}{4}\right)$$

$$+ U(x^+, \phi^-)\left(\frac{c_2}{2dx} - \frac{c_3}{2d\phi} + \frac{c_7}{4}\right) + U(x^-, \phi^-)\left(\frac{-c_2}{2dx} - \frac{c_4}{2d\phi} + \frac{c_8}{4}\right).$$

(A7)

The quantities a_1 and a_3 are defined by

$$a_1 \equiv \frac{-\sin \phi^+}{\rho(x)\xi(x) \cos \phi^+} + \frac{1}{2\xi^2(x)\rho(x) \cos \phi^+}\frac{\partial U_0}{\partial \phi}(x, \phi^+) - \frac{-\sin \phi^+}{2\xi^2(x)\rho(x) \cos^2 \phi^+} U_0(x, \phi^+),$$

(A8)

and

$$a_3 = \frac{1}{\rho(x^+)\xi^2(x^+)} - \frac{1}{2\xi^2(x^+)\rho(x^+) \cos \phi}\frac{\partial U_0}{\partial x}(x^+, \phi) + \frac{1}{2\xi^3(x^+)\rho(x^+) \cos (\phi)} U_0(x^+, \phi);$$

(A9)

a_2 is similar to a_1, with ϕ^- replacing ϕ^+ in equation (A8), and a_4 is similar to a_3, with x^- replacing x^+ in equation (A9). The b_i are defined by

$$b_1 = \frac{1}{\rho(x) \cos \phi},$$

(A10)

$$b_2 = \frac{1}{\rho(x)\xi^2(x) \cos \phi},$$

(A11)

$$b_3 = -\frac{1}{\rho^2(x^+)\cos\phi}\frac{d\rho(x^+)}{dx}, \tag{A12}$$

$$b_4 = b_3 \quad (\text{with } x^- \text{ replacing } x^+ \text{ in eq. [A12]}), \tag{A13}$$

$$b_5 = \frac{\sin\phi^+}{\rho(x)\xi^2(x)\cos^2\phi^+}, \tag{A14}$$

$$b_6 = b_5 \quad (\text{with } \phi^- \text{ replacing } \phi^+ \text{ in eq. [A14]}). \tag{A15}$$

The c_i are defined by

$$c_1 = \xi(x)\sin\phi^+ + \frac{\sin\phi^+}{\cos\phi^+}U_0(x, \phi^+), \tag{A16}$$

$$c_2 = c_1 \quad (\text{with } \phi^- \text{ replacing } \phi^+ \text{ in eq. [A16]}), \tag{A17}$$

$$c_3 = -\cos\phi - \frac{U_0(x^+, \phi)}{\xi(x^+)}, \tag{A18}$$

$$c_4 = c_3 \quad (\text{with } x^- \text{ replacing } x^+ \text{ in eq. [A18]}), \tag{A19}$$

$$c_5 \equiv C(x^+, \phi^+) = \frac{\sin\phi^+}{\cos\phi^-}\frac{\partial U_0}{\partial x}(x^+, \phi^+) - \frac{1}{\xi(x^+)}\frac{\partial U_0}{\partial\phi}(x^+, \phi^+), \tag{A20}$$

$$c_6 = C(x^-, \phi^+), \tag{A21}$$

$$c_7 = C(x^+, \phi^-), \tag{A22}$$

$$c_8 = C(x^-, \phi^-). \tag{A23}$$

II. MODIFIED EIGENVALUE PROBLEM

Equation (A6) represents a set of algebraic equations to be solved at all the grid array points of U. Similarly, equation (A7) represents a set of algebraic equations to be solved at all the grid array points of Ψ. We define the array $\hat{U}(i, j)$, formed from the values of $U(x, \phi)$ at the U grid points. $\hat{U}(i, j)$ is an $(l + 1) \times (m + 1)$ matrix. Similarly, we define the array $\hat{\Psi}(i, j)$, formed from the values of $\Psi(x, \phi)$ at the Ψ grid points. $\hat{\Psi}(i, j)$ is an $l \times m$ matrix. To reduce the problem to one dimension, the $\hat{U}$ and $\hat{\Psi}$ arrays are mapped to the column matrices $\hat{u}$ and $\hat{s}$ by

$$\hat{U}(i, j) \to \hat{u}(k_1) \qquad \text{with } k_1 = (i - 1)(l + 1) + j, \tag{A24}$$

and

$$\hat{\Psi}(i, j) \to \hat{s}(k_2) \qquad \text{with } k_2 = (i + 1)l + j. \tag{A25}$$

Equations (A6) and (A7) are written in matrix form, using the mapping defined in equations (A24) and (A25) as

$$i\lambda\hat{u} = \hat{A}\hat{s}, \tag{A26}$$

$$i\lambda\hat{B}\hat{s} = \hat{C}\hat{u}, \tag{A27}$$

where $\hat{A}$, $\hat{B}$, and $\hat{C}$ are two-dimensional matrices formed from the coefficients of $\hat{u}$ and $\hat{s}$ in equations (A6) and (A7). $\hat{A}$ is $(l + 1)(m + 1) \times lm$, $\hat{B}$ is $lm \times lm$, and $\hat{C}$ is $lm \times (l + 1)(m + 1)$. Equations (A26) and (A27) define a modified eigenvalue problem.

III. PROGRAM IMPLEMENTATION AND SOLUTION

Matrix equations (A26) and (A27) were solved as follows:
Step 1.—The linear system

$$\hat{B}\hat{X} = \hat{C} \tag{A28}$$

is solved for the $lm \times (l + 1)(m + 1)$ order matrix $\hat{X}$.
Step 2.—The $lm \times lm$ order matrix $\hat{D}$ is calculated from

$$\hat{D} = \hat{X}\hat{A}. \tag{A29}$$

Step 3.—The eigenvalue problem

$$-\lambda^2\hat{s} = \hat{D}\hat{s} \tag{A30}$$

is solved for λ^2 and $\hat{s}$.

Step 4.—The column matrix $\hat{\mathbf{u}}$ is calculated from

$$\hat{\mathbf{u}} = -i\lambda^- \hat{\mathbf{A}}\hat{\mathbf{s}} \;. \tag{A31}$$

The use of the public domain subroutines for solving linear equations in LINPACK and the subroutines for solving eigenvalue equations in EISPACK aided the implementation of steps 1 and 3. Once the programs were debugged, the solution procedure was completed without difficulty.

The program size and execution time are determined mainly by the grid resolution. The $l = 19$, $m = 43$ resolution requires the definition (within the program) of at least two arrays of the order 880×880. In single precision (FORTRAN) this represents six megabytes of storage. When only a selected number of the eigenfunctions are calculated, additional storage space is required to hold intermediate results, thereby further increasing storage requirements. For most of the runs, the program storage size was about eight megabytes. It is unlikely that this number can be reduced (other than by reducing the grid resolution). The execution time to calculate all 817 eigenfunctions is about 1600 minutes (CPU), on a VAX 11-750. This time would be reduced by 2 orders of magnitude if the program were run on one of NCAR's Cray computers (memory restrictions prevented us from doing this).

REFERENCES

Backus, G., and Gilbert, F. 1968, *Geophys. J.R.A.S.*, **16**, 169.
Bretherton, F. P. 1964, *Tellus*, **16**, 181.
Christensen-Dalsgaard, J., Gough, D. O., and Morgan, J. G. 1979, *Astr. Ap.*, **73**, 121.
Clement, M. J. 1981, *Ap. J.*, **249**, 746.
———. 1984, *Ap. J.*, **276**, 724.
Duvall, T. L., Jr., Dziembowski, W. A., Goode, P. R., Gough, D. O., Harvey, J. W., and Leibacher, J. W. 1984, *Nature*, **310**, 22.
Duvall, T. L., Jr., and Harvey, J. W. 1984, *Nature*, **310**, 19.
EISPACK, 1972, Eigensystem and Subroutine Package, NATS Project (Argonne: Argonne Code Center, Argonne National Laboratory).
Gilman, P. A. 1984, *Proc. Snowmass Conf. on Solar Seismology from Space*, ed. R. K. Ulrich, J. Harvey, E. J. Rhodes, Jr., and J. Toomre (Pasadena: Jet Propulsion Laboratory), p. 41.
Gilman, P. A., and Glatzmaier, G. A. 1981, *Ap. J. Suppl.*, **45**, 335.
Gilman, P. A., and Guenther, D. B. 1985, *Ap. J.*, in press (Paper II).
Gilman, P. A., and Miller, J. 1985, in preparation.
Glatzmaier, G. A. 1984, *J. Comput. Phys.*, in press.
Gough, D. O. 1984, *Observatory*, **104**, 118.
Greenspan, H. P. 1968, *The Theory of Rotating Fluids* (Cambridge: Cambridge University Press).
Iben, I., Jr., and Mahaffy, J. 1976, *Ap. J. (Letters)*, **209**, L39.
LINPACK, 1979, Linear Systems Subroutine Package (Argonne: National Energy Software Center, Argonne National Laboratory).
Munk, W., and Phillips, N. 1968, *Rev. Geophys.*, **6**, 447.
Saio, H. 1982, *Ap. J.*, **256**, 717.
Stern, M. E. 1963, *Tellus*, **15**, 246.
Stewartson, K. 1972, *Tellus*, **24**, 283.
Tolstoy, I. 1963, *Rev. Mod. Phys.*, **35**, 207.

PETER A. GILMAN: High Altitude Observatory, National Center for Atmospheric Research, P.O. Box 3000, Boulder, CO   80307

DAVID B. GUENTHER: Department of Astronomy, Yale University, P.O. Box 6666, New Haven, CT   06511